

See discussions, stats, and author profiles for this publication at: <https://www.researchgate.net/publication/258996560>

Simulation of Surface-Directed Phase Separation in a Solution-Processed Polymer/PCBM Blend

ARTICLE *in* MACROMOLECULES · NOVEMBER 2013

Impact Factor: 5.8 · DOI: 10.1021/ma400269j

CITATIONS

10

READS

56

2 AUTHORS:



Jasper J Michels

Max Planck Institute for Polymer Research

43 PUBLICATIONS 998 CITATIONS

[SEE PROFILE](#)



Ellen Moons

Karlstads universitet

74 PUBLICATIONS 4,006 CITATIONS

[SEE PROFILE](#)

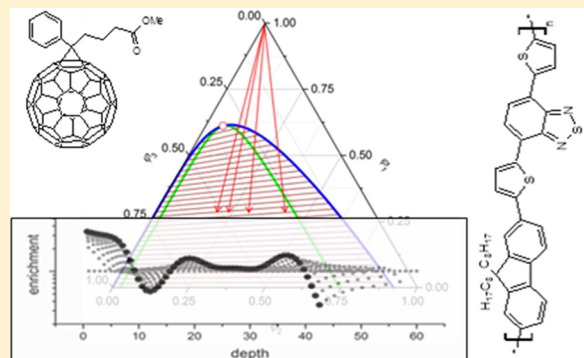
Simulation of Surface-Directed Phase Separation in a Solution-Processed Polymer/PCBM Blend

Jasper J. Michels^{†,*} and Ellen Moons[‡]

[†]Holst Centre/TNO, High Tech Campus 31, 5656 AE Eindhoven, The Netherlands

[‡]Department of Engineering and Physics, Karlstad University, SE-65188 Karlstad, Sweden

ABSTRACT: The formation of the surface-induced stratified lamellar composition profile experimentally evidenced in spincoated layers of the photovoltaic donor–acceptor blend consisting of poly[(9,9-diethylfluorenyl-2,7-diyl)-co-5,5-(4',7'-di-2-thienyl-2',1',3'-benzothiadiazole)]/phenyl-C61-butrylic acid methyl ester (APFO-3/PCBM), as processed from chloroform, is simulated using square gradient theory extended with terms describing the interaction of the blend components with the air and substrate interfaces. The surface energy contributions have been formulated based on an enthalpic nearest-neighbor model which allows integration of common surface tension theory and experimentally accessible surface energies of the fluid phase constituents with a mean field description of a multicomponent blend confined by substrate and air interfaces. Using estimates for the quench depth and transport properties of the blend components as a function of polymer concentration, the time-resolved numerical simulations yield results that compare favorably with experimental observations, both in terms of the number of lamellae as a function of the blend layer thickness and their compositional order. The effect of blend ratio is reproduced as well, the lamellar pattern becoming more pronounced if the amount of PCBM increases relative to APFO-3.



INTRODUCTION

Now that light-to-power conversion efficiencies of solution-processed organic bulk heterojunction photovoltaic (OPV) cells based on donor–acceptor blends reach values compatible with large scale application,^{1,2} there is an increasing need for making predictions on how the performance of solution processed OPV cells depends on blend material characteristics, solvent choice, and processing conditions. The key issue here is to understand how these parameters determine the final donor–acceptor phase morphology since phase domain size, shape, and percolation have major influence on device performance. The importance of morphological aspects in polymer (donor)/phenyl-C61-butrylic acid methyl ester (PCBM, acceptor) and polymer–polymer OPV blend layers has been widely acknowledged and recently been reviewed for a broad range of donor–acceptor combinations.^{3,4}

Donor–acceptor blend films of solution-processed OPV cells are typically prepared by a coating or printing technique characterized by solvent evaporation, sometimes followed by a thermal anneal. The final morphology of the layers can be a result of multiple phase transitions, which may occur during solution processing and/or annealing. The coating stage is characterized by a high molecular mobility owing to the presence of a considerable solvent fraction. In contrast, in case of annealing, mobilities are typically several orders of magnitude lower, mainly affecting short-ranged molecular order and crystallization.

As experimentally evidenced by studies involving a broad range of polymer/PCBM systems, ranging from traditional PPV-based systems,^{5,6} to blends containing more recent low band gap donor materials, such as alternating polyfluorene copolymers (APFO),^{7–9} and poly(diketo pyrrolopyrrole) (pDPP),^{10,11} but also in all-polymer OPV blends,^{12–14} if the evaporation rate of the accommodating solvent system of an OPV blend is sufficiently high, the blend may be solvent-quenched in or near the unstable region of the liquid state ternary phase diagram of solvent, donor, and acceptor. As a result, liquid-phase demixing, occurring via spinodal decomposition or nucleation-and-growth, will under those circumstances be the dominant mechanism of phase separation between the active blend components, often leading to characteristic drop-like domain structures resulting from capillary forces due to fluid–fluid interactions. The average domain size of such liquid phase demixed OPV blends typically exceeds the exciton diffusion length by at least an order of magnitude, thereby significantly reducing the charge separation probability of excitons at the donor–acceptor interface. Hence, these rather coarse morphologies do not give optimal device performance and should preferably be avoided. This is often accomplished by the use additives,^{15–20} such as *o*-dichlorobenzene (*o*-DCB) and 1,8-diiodooctane (DIO), and 1-

Received: February 8, 2013

Revised: October 4, 2013

Published: October 25, 2013

chloronaphthalene (CN),²¹ which generally reduce polymer solvation and promote chain aggregation and gelation.

Nevertheless, due to the fact that liquid phase demixing does not seem to yield the preferred phase separated morphology for most OPV applications, it is very important to be able to indicate and predict how it depends on processing parameters and in which region of “processing space” it is dominant. For this reason, it is unfortunate that the number of consistent studies giving theoretical insight into liquid phase demixing in OPV blends, while establishing the link with physical material- and processing parameters, is scarce.²² As a result, process optimization is still largely subject to time-consuming trial-and-error experimentation.

As is known from the field of classical polymers,²³ and later observed for functional polymer systems,^{24–26} liquid phase demixing within a thin solvent-borne fluid film supported by a substrate, occurs according to a distinct order of events. The process is called surface-directed spinodal decomposition (SDSD) and has been studied extensively (mostly though for binary polymer blends in the melt), both experimentally^{27–29,69–71} and theoretically.^{27,30–32,72} The topic of surface-induced effects on phase separation has been reviewed by several authors.^{33–35} In the early stages of SDSD preferential wetting of the substrate and/or air interface by one of the blend components induces vertical stratification into a lamellar ordering of the phases. In a later stage, lamellae may break up into droplets due to fluid–fluid interfacial instabilities. Finally, these droplets may merge into larger domains, eventually giving laterally separated phases. Whether or not lamellar break up indeed occurs during film processing depends on the mobility of the blend components in solution, which, in turn, is strongly dependent on polymer concentration. Because of continued solvent evaporation, the latter will increase, eventually vitrifying the system and kinetically freezing the phase morphology.

Using SIMS depth profiling, Moons et al. were the first to experimentally identify “frozen” vertically segregated multi-lamellar structures in solution-processed (nonannealed) OPV blend layers, i.e., consisting of vertically alternating regions enriched (depleted) and depleted (enriched) in polymer (PCBM). These morphologies were especially apparent in SiO_x -borne CHCl_3 -processed layers based on derivatives of poly[(9,9-dioctylfluorenyl-2,7-diyl)-co-5,5-(4',7'-di-2-thienyl-2',1',3'-benzothiadiazole)] (APFO-3) and PCBM.^{36–39} At the air and substrate interfaces, respective enrichment of APFO-3 and PCBM was consistently found, while the number of lamellae in the bulk showed a dependence on layer thickness: four lamellae were identified in case of a ~70 nm layer,³⁶ whereas up to six were observed for a ~150 nm thickness.³⁷ As concluded by the authors, the occurrence of multiple lamellae strongly indicates that these stratified morphologies form via SDSD. The encountered compositional preference at the SiO_x and air interfaces was qualitatively explained by the match between the surface energy of the substrate and the surface energies of the solid blend components.⁹

As indicated above, it is of interest both fundamentally and from an application point-of-view to be able to *a priori* identify processing conditions/material parameter combinations that allow for liquid phase demixing in OPV blends, as well as their generality. Recently, a study has appeared aiming at doing so using a square gradient approach,⁴⁰ which, though mathematically elegant, unfortunately does not seem to give a sufficiently accurate description of the physics involved to allow for proper

comparison with experimental observations, such as reported by Moons et al. First, although the model, which, apart from the number of space dimensions seems to be mostly a copy of an earlier modeling study,^{41,42} incorporates a description for substrate interactions (using arbitrary input), it omits contributions stemming from segregation at the air interface due to liquid–vapor surface tension differences. Second, the kinetic equations used in ref 40 are limited, as they only treat diagonal components of the mobility matrix. Clarke et al. recently published a similar solvent-based ternary square gradient model but with a properly defined mobility matrix,⁴³ however unfortunately lacking air- or substrate interactions.

This paper aims to further close the existing hiatus in the understanding morphology formation of solution-based OPV blends by making a much closer comparison with experimental data than the studies mentioned above. To this purpose, the SIMS results by Moons et al. form an excellent opportunity for modeling surface-directed effects in OPV blends, separate from late-stage breakup and lateral coarsening. In contrast to the reports mentioned above, both air and substrate interactions are taken into account in combination with the full mobility matrix as defined for a ternary system. Specifically, instead of defining a model only used to predict general trends as a function of arbitrarily chosen input, we aim to reproduce the lamellar phase morphologies experimentally observed for thin³⁶ (~70 nm) and thick³⁷ (~150 nm) silicon oxide-supported APFO-3/PCBM blend layers by using physical input data rather than arbitrary values. Air- and substrate contributions are cast into an interaction parameter formulation, fully compatible with well-established surface interaction theory in order to allow direct quantification via measurement or estimation of the surface energies of the individual blend components. We note that this approach is not limited to OPV blends, but may be considered general for demixing liquid blends with any number of components. Surface directed demixing in both thin and thick blend layers are simulated for different blend ratio's and results are discussed in view of the calculated ternary phase diagram for the $\text{CHCl}_3/\text{APFO-3}/\text{PCBM}$ blend. The simulated vertical composition profiles are thoroughly compared to the reported SIMS spectra.

THEORETICAL BASIS AND METHODOLOGY

Simulation of the dynamics of liquid-state phase separation of the ternary $\text{CHCl}_3/\text{APFO-3}/\text{PCBM}$ blend may be performed using Cahn–Hilliard theory, which requires the definition of a bulk free energy functional in conjunction with a kinetic model describing material transport. A common approach is to extend the homogeneous (local) free energy of mixing with nonlocal terms representing the free energy penalty associated with the formation of gradients in composition. For an n -component system this free energy functional reads:^{43–45}

$$F = \int dV \left[f_0(\varphi_i) + \frac{1}{2} \sum_{i=1}^n \kappa_i (\nabla \varphi_i)^2 \right] \quad (1)$$

Here, φ_i represents the volume fraction of the i th component, and κ_i are gradient energy coefficients. Following Clarke's approach,⁴³ κ_i is approximated using de Gennes' formulation⁴⁶ based on the random phase approximation (in units of kT): $\kappa_i = a^2/(18\varphi_i)$, with a representing a Kuhn length. The local free energy $f_0(\varphi_i)$ may be given by the Flory–Huggins model. As mentioned, eq 1 solely represents the free energy of the bulk solution.

Inclusion of air and substrate interactions is achieved by augmenting the bulk free energy with terms describing free energy contributions stemming from interaction with external interfaces. The formulation most commonly used for this purpose^{47,48,51} is the one suggested by Puri, Binder, and Frisch,⁴⁹ which relies on the definition of a bare surface energy, written as a quadratic function of volume fraction and two coefficients, usually denoted as μ_1 (or h_1) and g , that characterize the static surface phase diagram. Although in crude argumentation g and μ_1 have been related to measurable data, such as surface energy and interaction parameter,⁴⁷ they are usually assigned arbitrary values.⁵⁰

Here we follow an approach that straightforwardly extends the local bulk free energy with extra sets of binary interaction parameters (χ) describing the nearest-neighbor interactions between the blend components and the substrate- as well as the air interface. In Flory–Huggins terminology⁵¹ an interaction parameter is an exchange parameter, written as a function of the interaction energies (ϵ) between like and unlike monomers or segments, the lattice (bulk) coordination number (z), and kT :

$$\chi_{ij} = \frac{z}{kT} \left[\epsilon_{ij} - \frac{1}{2} (\epsilon_{ii} + \epsilon_{jj}) \right] \quad (2)$$

Analogously, binary interaction parameters may be defined for the interaction of the blend components with the air- (subscript a) and substrate (subscript s) interfaces:

$$\chi_{ia} = \frac{z}{kT} \left[\epsilon_{ia} - \frac{1}{2} (\epsilon_{ii} + \epsilon_{aa}) \right] \quad (3)$$

$$\chi_{is} = \frac{z}{kT} \left[\epsilon_{is} - \frac{1}{2} (\epsilon_{ii} + \epsilon_{ss}) \right] \quad (4)$$

Bond cutting arguments⁴⁷ allow the interaction energies ϵ_{ia} and ϵ_{is} to be written in terms of surface energies γ_i and γ_s :

$$\epsilon_{ii} = 2\epsilon_{ia} = \frac{2b^2\gamma_i}{z'} \quad \text{and} \quad \epsilon_{ss} = \frac{2b^2\gamma_s}{z'} \quad (5)$$

Here, b is the length of one lattice site and z' is the surface coordination number. As the interaction with the substrate involves the formation (or breaking) of the physical “bond” between a fluid segment and the substrate, ϵ_{is} is related to the work of adhesion W_i :

$$\epsilon_{is} = \frac{W_i b^2 \gamma_i}{z'} \quad (6)$$

W_i is for instance given by the disperse (superscript d) and polar (superscript p) surface energy contributions of fluid and substrate:^{52,53}

$$W_i = 2(\sqrt{\gamma_i^d \gamma_s^d} + \sqrt{\gamma_i^p \gamma_s^p}) \quad (7)$$

Substitution of eqs 5, 6 and 7 in eqs 3 and 4 and respecting conventions of sign yields:

$$\chi_{ia} = \frac{zb^2\gamma_i}{z'kT} \quad (8)$$

$$\chi_{is} = \frac{zb^2}{z'kT} [\gamma_i + \gamma_s - 2(\sqrt{\gamma_i^d \gamma_s^d} + \sqrt{\gamma_i^p \gamma_s^p})] \quad (9)$$

The part between square brackets in eq 9 represents the interfacial tension between fluid and substrate. Advantageously, this approach provides a practical and direct link between

measurable surface energy data and physical input data for the square gradient model. Nevertheless, this approach is approximate as it only involves enthalpic nearest neighbor effects. Entropic contributions to the air and substrate interactions are not taken into consideration.

The extended Flory–Huggins free energy per lattice site is now written in units of kT as:

$$f_0(\varphi_i) = \sum_{i=1}^n \frac{\varphi_i}{N_i} \ln(\varphi_i) + \sum_{i=1}^{n-1} \sum_{j>i}^n \chi_{ij} \varphi_i \varphi_j + \sum_{i=1}^n \chi_{ia} \varphi_i \varphi_a \\ + \sum_{i=1}^n \chi_{is} \varphi_i \varphi_s \quad (10)$$

In eq 10 the air and substrate are treated as two additional blend components represented by “volume fractions” φ_a and φ_s which are only nonzero at sites adjacent to the respective interfaces. The first two terms in eq 10 represent the usual bulk form with N_i the effective degrees of polymerization of the blend components and χ_{ij} the binary interaction parameters. As the exact physical values for φ_a , φ_s , z , and z' are not straightforwardly evident,⁴⁷ we recast the surface interaction terms and write:

$$f_0(\varphi_i) = \sum_{i=1}^n \frac{\varphi_i}{N_i} \ln(\varphi_i) + \sum_{i=1}^{n-1} \sum_{j>i}^n \chi_{ij} \varphi_i \varphi_j \\ + w(\sum_{i=1}^n \chi_{ia}^0 \varphi_i + \sum_{i=1}^n \chi_{is}^0 \varphi_i) \quad (11)$$

The multiplication factor w is given by: $w = (z\varphi_a/z') = (z\varphi_s/z')$, and:

$$\chi_{ia}^0 = \frac{b^2 \gamma_i}{kT} \quad (12)$$

$$\chi_{is}^0 = \frac{b^2}{kT} [\gamma_i + \gamma_s - 2(\sqrt{\gamma_i^d \gamma_s^d} + \sqrt{\gamma_i^p \gamma_s^p})] \quad (13)$$

The parameter w effectively defines how the air and substrate contributions compare to the interactions between adjacent sites in the bulk. In this study we treat w as a “fitting parameter” and establish its value via a best match comparison between simulation results and experimental SIMS data; w is kept constant and equal for all calculations.

The development of the phase morphology in the blend layer as a function of time is accessed by numerically solving the set of kinetic Cahn–Hilliard equations.^{54,55} Assuming incompressibility and taking the solvent as the dependent component yields the following set of equations:

$$\frac{\partial \varphi_i}{\partial t} = \nabla \cdot \sum_{j \neq i} \Lambda_{ij} \nabla (\mu_i - \mu_j) + \zeta_i \quad (14)$$

Here, ζ_i represents the Langevin fluctuations^{56,57} and the quantity μ_i is given by the Euler–Lagrange equation: $\mu_i = (\delta F / \delta \varphi_i) = (\partial f / \partial \varphi_i) - (\nabla \partial f / \partial (\nabla \varphi_i))$, with f being the integrand of eq 1. Following refs 45 and 58, the Onsager coefficients Λ_{ij} are defined using Kramer’s vacancy flux theory⁵⁹ yielding the following expressions by combining eq 14 with the Gibbs–Duhem condition ($\sum_i \varphi_i \nabla \mu_i = 0$):

$$\begin{aligned}\Lambda_{ii} &= (1 - \varphi_i)^2 M_i + \varphi_i^2 \sum_{j \neq i} M_j \\ \Lambda_{ij} = M_{ji} &= -(1 - \varphi_i)\varphi_j M_i - (1 - \varphi_j)\varphi_i M_j \\ &+ \varphi_i\varphi_j \sum_{k \neq i, j} M_k\end{aligned}\quad (15)$$

Here, M_i denotes the mobility coefficients of the individual blend components. Different approaches to defining Λ_{ij} exist, but Kramer's theory has shown to reproduce experimental data most satisfactorily.⁶⁰ We note here that this treatment takes into account the full mobility matrix, which yields a more realistic and complete representation of the phase separation dynamics than do the models by Wodo⁴⁰ and Saylor,^{41,42} which only consider the diagonal components.

In the preceding section, the evolution equations have been defined for an n -component blend. In what follows, focus shall be on the actual *ternary* blend of CHCl₃/APFO-3/PCBM, of which the individual blend constituents are respectively indicated as components "1", "2", and "3". A suitable transport theory relates the mobilities of the individual components M_i to a general monomeric diffusivity D_0 considered equal for all components.^{43,45} Vitrification of the blend as a result of the rise in T_g during evaporation is not taken into account.⁴³ The mobility of the solvent is given by: $M_1 = D_0\varphi_1$. Given the fact that liquid phase demixing in the CHCl₃/APFO-3/PCBM blend is likely to take place in the semidilute or concentrated regime, hydrodynamic interactions can be considered screened, suggesting the Rouse model to be appropriate to describe the dynamics of the polymer. The effect of entanglements is considered negligible due to the relatively low molecular weight of APFO-3,⁹ in combination with its semiflexible nature.

The mobility of APFO-3 (M_2) is estimated by regarding the polymer chain as a sequence of Kuhn segments or sites, each with an effective radius of $R \sim a/2$ and diffusivity D_0R_1/R , with R_1 being the radius of a solvent (CHCl₃) molecule ($= (3V_{m,1}/(4\pi N_A v))^{1/3} \sim 0.3$ nm). Hence

$$M_2 = \frac{2R_1D_0}{aN'_2}\varphi_2 \quad (16)$$

Here, N'_2 represents the effective degree of polymerization in terms of the (average) number of Kuhn segments per chain (estimated to be ~ 13 based on the molecular weight⁹ and estimated Kuhn length (see below)). A PCBM molecule is considered as a hard sphere exceeding the dimensions of a solvent molecule. We define its mobility by

$$M_3 = \frac{R_1D_0}{R_3}\varphi_3 \quad (17)$$

Here, $R_3 \sim 0.6$ nm, as obtained from the molecular volume of PCBM.⁶¹

Finally, solvent evaporation is implemented by decreasing φ_1 from the top surface of the wet film at a rate proportional to the local average solvent volume fraction and a (relative) liquid-to-vapor mass transfer coefficient: $r = r_0\bar{\rho}_1$. Following previous methods,^{41–43} all length and time scales are nondimensionalized by expressing them in units of characteristic values a and $\tau = a^2/D_0$. The nondimensionalized liquid-to-vapor mass transfer coefficient is given by $\tilde{r}_0 = r_0a^2/D_0$. As shown by Wodo,⁴⁰ the dimensionless evaporation rate is more practically written as a Biot number $Bi = r_0L^2/D_0$, which conveniently expresses the balance between the rates of solvent evaporation and mass

transport. Here, L is the initial wet layer thickness at the start of each simulation.

The nondimensional forms of eqs 14 are numerically integrated in one space dimension, i.e. the z -direction, using a standard explicit finite difference protocol. The grid spacing is defined by the Kuhn length a and no-(fluid)-flux boundary conditions apply to the air and substrate interfaces. The decrease in fluid layer thickness due to solvent evaporation at $t > 0$ is achieved by scaling the grid spacing with the average amount of residual solvent for each time step, thus assuring mass conservation of the solid components. In this study the noise terms in eqs 15 are omitted, as the low measured dry film roughness of vertically stratified APFO/PCBM blends²⁸ suggests that the system vitrifies in the lamellar stage during which surface-directed effects dominate the influence of thermal fluctuations.

RESULTS AND DISCUSSION

All parameters (i.e., N_i and χ_{ij}) that determine the bulk contribution of the local free energy of the CHCl₃/APFO-3/PCBM blend are taken from ref 9 and listed in Table 1. The effective degrees of polymerization are obtained by treating one solvent molecule as one lattice site and scaling the other components accordingly, as described in ref 9.

Table 1. Effective Degrees of Polymerization and Interaction Parameters for the Ternary Blend Consisting of CHCl₃, APFO-3, and PCBM

	N_i		χ_{12}	χ_{13}	χ_{23}
CHCl ₃	1	CHCl ₃ /APFO-3/PCBM	0.505	0.885	0.4
APFO-3	66				
PCBM	5				

Figure 1 presents the ternary phase diagram of the CHCl₃/APFO-3/PCBM blend, calculated using the input from Table 1. The critical point, spinodal and binodal compositions are

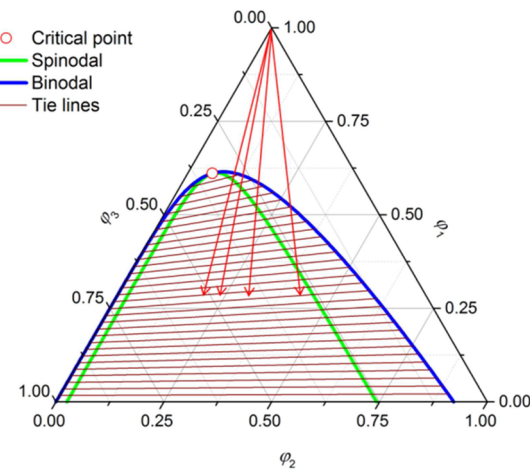


Figure 1. Ternary phase diagram of the blend CHCl₃/APFO-3/PCBM (indicated by component 1, 2, and 3, respectively), calculated using Flory–Huggins theory; volume fractions of the three components are indicated on the axes; the green and blue lines respectively represent the binodal and spinodal compositions; tie lines (brown) connect binodal compositions at the same chemical potential; the arrows indicate the directions of the solvent quench for a (from right to left) 1:1, 1:2, 1:3, and 1:4 (w/w) APFO-3/PCBM ratio.

indicated by the red circle, green, and blue lines, respectively. The tilt angle of the tie lines (brown) is mostly dictated by the enthalpic difference (*i.e.* χ_{12} and χ_{13}) in compatibility with chloroform between APFO-3 and PCBM and expresses the partitioning of the solvent between the phases. In contrast, the pronounced asymmetry in the phase diagram is of entropic origin, as it is explained by the considerable size difference between APFO-3 and PCBM. As a result, the phase diagram shows that the binodal compositions enriched in APFO-3 still contain a significant fraction of PCBM, whereas the PCBM-enriched binodal compositions are much more pure.

A first observation is that the compatibility between APFO-3 and PCBM is sufficiently high to only allow liquid phase demixing to take place at high solids concentration (*i.e.*, $(\varphi_2 + \varphi_3) > 0.37$). This may explain why the “kinetically frozen” lamellar profiles could be obtained experimentally, as vitrification may have frustrated or even fully prevented breakup and lateral coarsening. This conclusion is supported by the low surface roughness, as measured by atomic force microscopy (AFM) of the blend layer (~ 2.5 nm).³⁷ In contrast, in case of blends characterized by a significantly higher χ_{23} (*e.g.*, in poly(9,9'-dioctylfluorene) (PF)/PCBM and poly[(9,9-dioctylfluorenyl-2,7-diyl)-*alt*-co-(N,N'-diphenyl-N,N'-di(*p*-butylphenyl)-1,4-diaminobenzene)] (PFB)/PCBM),^{8,9} the critical point corresponds to a much higher solvent fraction, thus allowing sufficient mobility for breakup and coarsening to take place before vitrification, resulting in drop-like lateral phase morphologies giving a considerably higher AFM roughness.⁹ The fact that for CHCl₃/APFO-3/PCBM the unstable part of the phase diagram corresponds to a quite concentrated regime strongly suggests that material transport during phase separation is likely to be dominated by diffusion and that possible phenomena related to fluid flow can be neglected.

The red arrows in Figure 1 illustrate the change in composition upon solvent evaporation for blend ratios (APFO-3/PCBM w/w) 1:1, 1:2, 1:3, and 1:4 (from right to left), *i.e.*, corresponding to the experimental ratios used for the SIMS analyses by Moons et al.^{36,37} Although the exact point of vitrification (or “freezing”) for each blend ratio is unknown, the arrows show that blends with a high PCBM fraction (relative to APFO-3), cross the spinodal at a higher solvent volume fraction than blends with a high relative amount of polymer. Furthermore, it is observed that for a similar quench depth in the unstable region the latter compositions would be closer to the spinodal line than the former, therefore having a less negative curvature in the free energy and hence exhibiting retarded de-mixing kinetics. As will be shown by the simulations, whether or not the blend is quenched near the spinodal line will have a pronounced effect on surface-induced phase separation and interfacial enrichment.

Table 2 lists measured and estimated values for the total, disperse and polar surface energy of the blend components and

the SiO_x substrate. Work of adhesion and fluid-substrate interfacial tensions are also listed, together with calculated values for the air- and substrate interaction parameters χ_{ia} and χ_{is} . The disperse and polar surface energy contributions of the silicon oxide substrate have been experimentally determined,^{62,63} while the values for chloroform were taken from literature.⁶⁴ The total surface energies of APFO-3 and PCBM have been reported earlier.⁹ We attempt to give reasonable estimates for their respective disperse and polar contributions, taking into account the relatively high saturated alkyl fraction of the APFO-3 chains, which usually depresses the polar contribution.⁶⁵

The interaction parameters χ_{ia} and χ_{is} obtained using $b = (V_m^{\text{CHCl}_3}/N_A)^{1/3} \sim 5$ Å and assuming a cubic lattice: $z = 6$ and $z' = 1$, show that the lowest surface free energy penalties are associated with enrichment of the solvent and PCBM at, respectively, the air and substrate interface, and that the order of preference is: CHCl₃ > APFO-3 > PCBM (air) and PCBM ≫ CHCl₃ ~ APFO-3 (substrate). This result is in agreement with the experimental observations.^{36,37} It is furthermore shown that χ_{ia} generally exceeds χ_{is} due to the fact that the sign conventions used for work of adhesion and surface energy are opposite (see eqs 12 and 13). Hence, the interaction with the substrate compensates for the free energy penalty resulting from the missing neighbor effect. Nevertheless, some care should be taken as it is not clear whether the assumption of equal z' for the air- and substrate interface is fully reasonable.

Combining the thermodynamic and kinetic input, the square gradient model is used to produce simulated vertical density distributions for the thin and thick blend films. At the start of each simulation ($t = 0$) the blend solution is assumed to be just above its critical point, by taking $\varphi_1(t = 0) = 0.63$, ensuring full miscibility (give or take some uncertainty due to the limited accuracy of mean field theory in the vicinity of the critical point) while at the same time representing a sufficiently high polymer concentration to allow neglect of hydrodynamic effects. Since it is not straightforward to establish the actual balance between the time scales of evaporation and diffusion in the real system, we resort to simulating demixing as a function of a range for Bi going from a diffusion-dominated scenario ($Bi \sim 0.1$), via a more or less balanced situation ($Bi \sim 1$) to an evaporation-dominated regime ($Bi \sim 10$), *i.e.* similar to the approach taken by Wodo et al.⁴⁰ The simulation results are then compared in order to establish which regime best represents the experimental SIMS traces.

Figure 2 presents the time-resolved simulated cross sectional profiles for different values of Bi for donor:acceptor (w/w) blend ratios 1:1, 1:2, 1:3, and 1:4 (thin layer: rows a–d) and 1:4 (thick layer: row e), plotted in terms of the APFO-3 volume fraction (φ_2) as a function of the z -coordinate. The data has been plotted on a semilogarithmic scale in order to facilitate comparison with SIMS spectra (see below). The gray curves represent concentration profiles at early times and the black lines correspond to the final snap shots of the situation, when about half of the initial solvent fraction has evaporated. In other words, the simulations for $Bi = 0.1$, *i.e.* corresponding to a low evaporation rate, ran for a ten times longer time than the ones corresponding to $Bi = 1$ and a hundred times longer time than for $Bi = 10$. In all cases the weighting factor for surface and substrate interactions is set to $w = 0.12$.

A first observation is that irrespective of the magnitude of Bi , structure formation is most pronounced for blends containing a high relative PCBM content (*i.e.*, 1:3 and 1:4 w/w ratio). The

Table 2. Surface Energy Data and Surface Interaction Parameters of the Ternary Blend CHCl₃/APFO-3/PCBM on SiO_x

	γ_{tot} (mN/m)	γ_d (mN/m)	γ_p (mN/m)	W_i (mN/m)	χ_{ia}	χ_{is}
SiO _x	53.5	36.5	17	(107)	—	—
CHCl ₃	27.5	25.9	1.6	71.9	10.2	3.4
APFO-3	32	31	1	75.5	11.9	3.7
PCBM	38	34	4	86.9	14.1	1.9

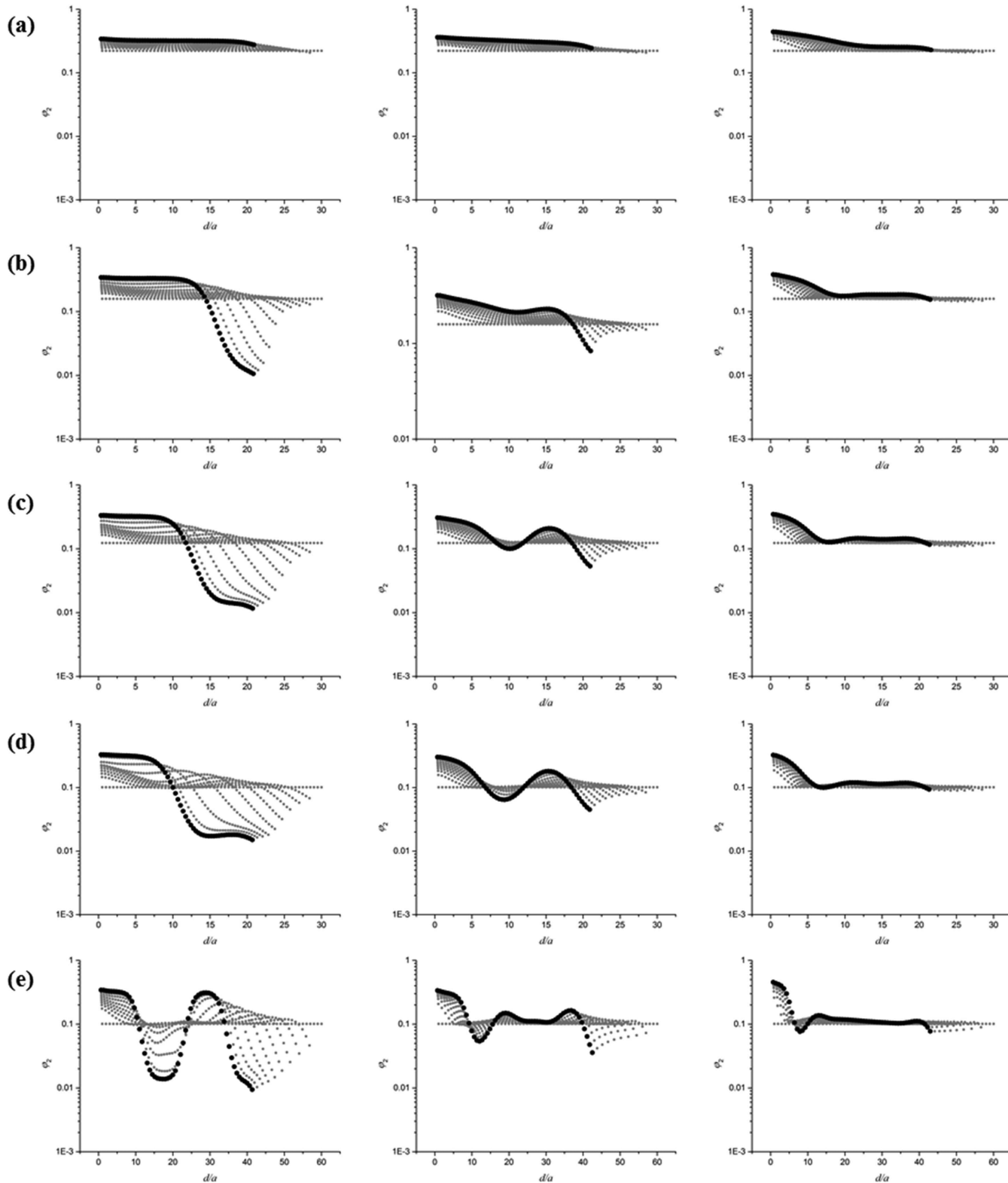


Figure 2. Simulated APFO-3 volume fraction (ϕ_2) plotted as a function of vertical coordinate expressed as multiples of the Kuhn length a (left, air; right, SiO_x) for blends corresponding to a thin ($\sim 70 \text{ nm}$) dry layer (rows a–d) and a thick ($\sim 150 \text{ nm}$) dry layer (row e) with APFO-3:PCBM ratio's (w/w) of 1:1 (row a), 1:2 (row b), 1:3 (row c), and 1:4 (rows d and e), obtained for Biot numbers ($Bi = r_0 L^2 / D_0$) $Bi \sim 0.1$ (left column), $Bi \sim 1$ (middle column), and $Bi \sim 10$ (right column). The dotted curves correspond to different time steps in the simulation: the profile corresponding to the final time step in the simulation is indicated in black; profiles at earlier times are indicated in gray.

explanation for this, as already hinted above, is the fact that for these blend ratios the solvent quench occurs well inside the unstable region of the phase diagram, corresponding to a

significantly higher negative curvature in the free energy of mixing than for blends with a high relative polymer content. Hence, the growth rate of (surface-induced) density

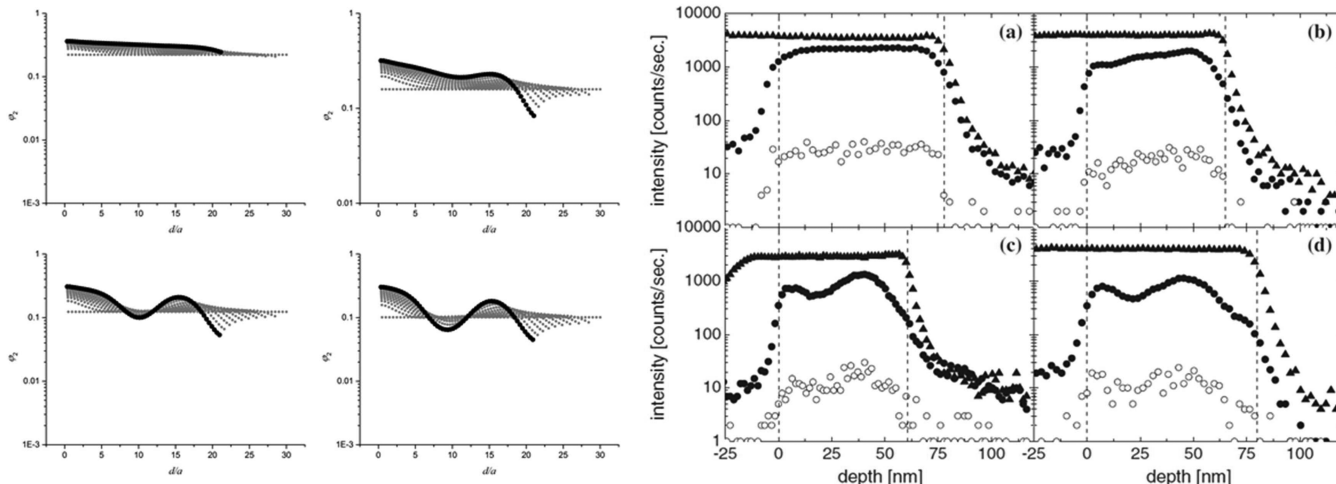


Figure 3. Left: Simulated APFO-3 volume fraction (ϕ_2) plotted as a function of vertical coordinate expressed as multiples of the Kuhn length a (air; right, SiO_x) for blends corresponding to a thin ($\sim 70 \text{ nm}$) dry layer with an APFO-3:PCBM ratio (w/w) of 1:1 (top left), 1:2 (top right), 1:3 (bottom left), and 1:4 (bottom right), obtained for $Bi \sim 1$; the dotted curves correspond to different time steps in the simulation: the profile corresponding to the final time step in the simulation is indicated in black; profiles at earlier times are indicated in gray. Right: intensity versus depth profiles of negative ions with different m/q ratios: 24 (C_2^-), solid triangles; 26 (CN^-), solid circles; 32 (S^-), open circles; obtained for thin ($\pm 70 \text{ nm}$) APFO-3/PCBM films on Si substrates. APFO-3 to PCBM blend ratios are (a) 1:1, (b) 1:2, (c) 1:3, and (d) 1:4 (w/w). The dotted lines indicate the depths at which the CN^- signal has increased to 50% of its saturation value (left) and where the C_2^- signal has fallen to 50% of its maximum value (right). The right-hand side and its caption have been reproduced from ref 36 with permission. Copyright 2010 IOP Publishing Ltd.

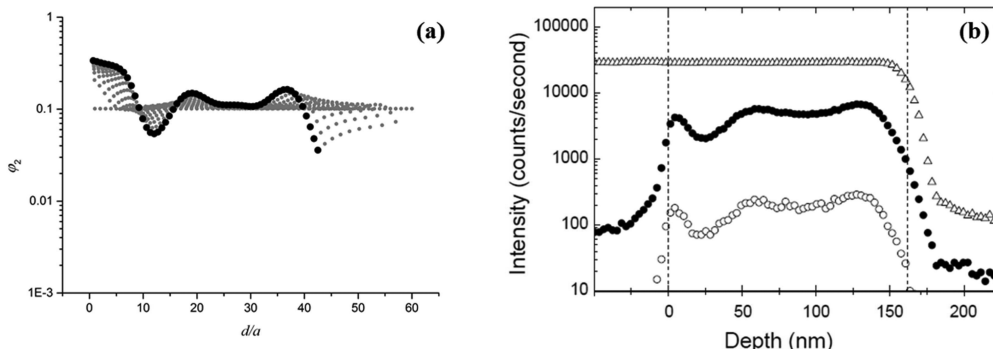


Figure 4. (a) Simulated APFO-3 volume fraction (ϕ_2) plotted as a function of vertical coordinate expressed as multiples of the Kuhn length a (air: left, SiO_x substrate: right) for a blend corresponding to a thick ($\sim 150 \text{ nm}$) dry layer with an APFO-3:PCBM ratio (w/w) of 1:4, obtained for $Bi \sim 1$; the dotted curves correspond to different time steps in the simulation: the profile corresponding to the final time step in the simulation is indicated in black; profiles at earlier times are indicated in gray. (b) Intensity versus depth profiles of negative ions with different m/q ratios: 24 (C_2^-), solid triangles; 26 (CN^-), solid circles; 32 (S^-), open circles, obtained for a thick ($\sim 150 \text{ nm}$) APFO-3/PCBM film on a Si substrate; APFO-3 to PCBM blend ratios is 1:4 (w/w). The dashed lines indicate the depths at which the CN^- signal has increased to 50% of its saturation value (left) and where the C_2^- signal has fallen to 50% of its maximum value (right). Part b and its caption have been reproduced from ref 37 with permission. Copyright 2006 SPIE.

perturbations is more enhanced in case of the former. A contributing factor is provided by the fact that for high-polymer blend ratios the overall kinetics are further decreased by a lower average mobility.

Second, not much differentiation is observed in a fast evaporation regime ($Bi = 10$), which suggestss that the still significant air-interface enrichment of APFO-3 in this case is kinetically determined rather than thermodynamically: the mobility of the polymer is simply too low to allow for evaporation-induced concentration gradients extending into the bulk of the film. In contrast, if $Bi = 0.1$ (low evaporation rate) thermodynamics prevail and the more segregated systems at high PCBM content are given sufficient time to further lower their free energy by collapsing lamellae into a reduced number of stratified phases. As a result, the final profiles for the 1:2, 1:3 and 1:4 blends in the thin layer configurations eventually all

effectively represent a bilayer structure at the end of the simulation. In case of the thick 1:4 blend layer for $Bi = 0.1$, the initial five or six lamellae collapse into a four layer pattern, the width of a single lamella considerably exceeding the lamellar width in a thin 1:3 or 1:4 blend layer.

In order to facilitate comparison between the simulated concentration profiles in Figure 2 and the SIMS ion yield profiles reported for thin and thick APFO-3/PCBM blend layers, the latter have been reproduced in this paper in Figures 3 and 4, respectively. Comparing the simulated APFO-3 volume fraction profiles with the ion traces corresponding to the CN^- ion (i.e., mainly indicative of the presence of the polymer) reveals that the calculated curves obtained for $Bi \sim 1$ best resemble the experimental data for all blend ratios, for both the thin and the thick blend layers. For this reason, the simulation results obtained for $Bi \sim 1$ have been replotted in

Figure 3 for the thin blend layers (four different blend ratio's) and in Figure 4 for the thick layer (only 1:4 w/w blend ratio). Indeed, both simulation and experiment show more pronounced lamellar morphologies at increased relative PCBM content, for reasons given above.

The experimentally observed numbers of lamellae in the thin and thick blend layers are reproduced for $0.3 < \chi_{23} < 0.45$ in conjunction with $3 \text{ nm} < a < 6 \text{ nm}$. The latter range exceeds the value of $a = 1 \text{ nm}$, typically encountered for flexible polymers,⁶⁶ which is plausible considering the semiflexible nature of the conjugated backbone of APFO-3. For comparison, the Kuhn lengths of regiorandom and region-regular P3HT have been determined to be 4 and 6 nm.^{67,68} Higher values for χ_{23} only allow representation of the experimental profiles (be it less accurately) if a is further increased, which we deem less realistic.

Comparison of the air-interfacial region of the simulated results and the SIMS traces reveals a marked difference between simulation and experiment in the sense that the ion counts consistently drop of more rapidly than the calculated volume fraction, showing less surface enrichment of polymer than suggested by the simulations. This difference is partly explained by the somewhat limited depth resolution of the SIMS analysis (i.e., $\sim 10 \text{ nm}$). As a result, the chemical information from the top region of the blend layer is effectively diluted as it coincides with secondary ions emerging from the interfacial region of the sacrificial polystyrene layer which is applied on top of the blend prior to analysis.³⁶ We further observe that especially for the 1:2 blend the simulated profile shape deviates somewhat with respect to the direction in which it is "tilted". Furthermore, for this blend ratio the simulated depletion at the substrate seems more extensive than suggested by the experiment. Explanations for these discrepancies are presently not evident.

CONCLUSIONS

It has been shown in this work that the experimentally observed surface-directed phase separation of solvent-quenched photovoltaic blends based on APFO-3 and PCBM can be at least qualitatively understood in terms of a square gradient model involving a Flory–Huggins-based description for the mixing free energy. Via a straightforward protocol based on bond cutting arguments, nearest neighbor air- and substrate interface interaction parameters are calculated for all components of the ternary blend $\text{CHCl}_3/\text{APFO-3}/\text{PCBM}$ using measured or estimated surface energy data. The resulting surface free energy contributions supplement the homogeneous bulk free energy and model segregation at the air- as well as the substrate interface. Demixing is triggered at the interfaces, which in case the composition is unstable, leads to the formation of multiple horizontally oriented lamellar regions alternatingly depleted and enriched in polymer or PCBM. Time-resolved numerical simulations for a range of Biot numbers (indicating the balance between the time scales of evaporation and diffusion): $0.1 < Bi < 10$ yield lamellar density profiles, which in case $Bi \sim 1$ compare favorably with (compositional) ion count depth profiles obtained with SIMS analysis. In agreement with the experimental SIMS profiles, the amplitude of the simulated lamellar density fluctuations enhances with increasing relative amount of PCBM. By means of the calculated ternary phase diagram it is shown that the enhanced demixing in case of a high relative amount of PCBM is caused by the fact that upon solvent evaporation the blend composition readily reaches the unstable region at a considerable distance from the spinodal

line. In contrast, in case of a high relative amount of polymer the quench leads to compositional changes in the vicinity of the stability limit, which strongly retards the phase separation kinetics.

AUTHOR INFORMATION

Corresponding Author

*E-mail: (J.J.M.) Jasper.michels@tno.nl.

Notes

The authors declare no competing financial interest.

ACKNOWLEDGMENTS

Prof. A. Budkowski and Dr. J. S. Gabel are kindly acknowledged for fruitful discussion. Ir. Charley Schaefer is kindly acknowledged for calculating and constructing the ternary phase diagram depicted in Figure 1. E.M. acknowledges the financial support from the Swedish Research Council (contract No. 621-2010-4155) and the Göran Gustafsson Foundation for Research in Natural Sciences and Medicine.

REFERENCES

- (1) He, Z.; Zhong, C.; Huang, X.; Wong, W. Y.; Wu, H.; Chen, L.; Su, S.; Cao, Y. *Adv. Mater.* **2011**, *23*, 4636.
- (2) Green, M. A.; Emery, K.; Hishikawa, Y.; Warta, W.; Dunlop, E. *Prog. Photovolt.: Res. Appl.* **2011**, *19*, 565.
- (3) Moulé, A. J.; Meerholz, K. *Adv. Func. Mater.* **2009**, *19*, 3028.
- (4) Liu, F.; Gu, Y.; Jung, J. W.; Jo, W. H.; Russel, T. P. *J. Polym. Sci., Part B: Polym. Phys.* **2012**, *50*, 1018.
- (5) Yang, X.; van Duren, J. K. J.; Janssen, R. A. J.; Michels, M. A. J.; Loos, J. *Macromolecules* **2004**, *37*, 2151.
- (6) Hoppe, H.; Niggeman, M.; Winder, C.; Kraut, J.; Hiesgen, R.; Hinsch, A.; Meissner, D.; Sariciftci, N. S. *Adv. Funct. Mater.* **2004**, *14*, 1005.
- (7) Barrau, S.; Andersson, V.; Zhang, F.; Masisch, S.; Bijleveld, J.; Andersson, M. R.; Inganäs, O. *Macromolecules* **2009**, *42*, 4646.
- (8) Björström, C. M.; Magnusson, K. O.; Moons, E. *Synth. Met.* **2005**, *152*, 109.
- (9) Nilsson, S.; Bernasik, A.; Budkowski, A.; Moons, E. *Macromolecules* **2007**, *40*, 8291.
- (10) Wienk, M. M.; Turbiez, M.; Gilot, J.; Janssen, R. A. J. *Adv. Mater.* **2008**, *20*, 2556.
- (11) Bijleveld, J. C.; Gevaerts, V. S.; Di Nuzzo, D.; Turbiez, M.; Mathijssen, S. G. J.; de Leeuw, D. M.; Wienk, M. M.; Janssen, R. A. J. *Adv. Mater.* **2010**, *22*, 242.
- (12) Arias, A. C.; MacKenzie, J. D.; Stevenson, R.; Halls, J. J. M.; Inbasekaran, M.; Woo, E. P.; Richards, D.; Friend, R. H. *Macromolecules* **2001**, *34*, 6005.
- (13) Arias, A. C.; Corcoran, N.; Banach, M.; Friend, R. H.; MacKenzie, J. D.; Huck, W. T. S. *Appl. Phys. Lett.* **2002**, *80*, 1695.
- (14) McNeil, C. R.; Watts, B.; Thomsen, L.; Belcher, W. J.; Greenham, N. C.; Dastoor, P. C. *Nanolett.* **2006**, *6*, 1202.
- (15) Huang, Y.; Guo, X.; Liu, F.; Huo, L. J.; Chen, Y. N.; Russell, T. P.; Han, C. C.; Li, Y. F.; Hou, J. H. *Adv. Mater.* **2012**, *24*, 3383.
- (16) Amb, C. M.; Chen, S.; Graham, K. R.; Subbiah, J.; Small, C. E.; So, F.; Reynolds, J. R. *J. Am. Chem. Soc.* **2011**, *133*, 10062.
- (17) Price, S. C.; Stuart, A. C.; Yang, L. Q.; Zhou, H. X.; You, W. J. *Am. Chem. Soc.* **2011**, *133*, 4625.
- (18) Chu, T. Y.; Lu, J. P.; Beaupre, S.; Zhang, Y. G.; Pouliot, J. R.; Wakim, S.; Zhou, J. Y.; Leclerc, M.; Li, Z.; Ding, J. F.; Tao, Y. *J. Am. Chem. Soc.* **2011**, *133*, 4250.
- (19) Huo, L. J.; Zhang, S. Q.; Guo, X.; Xu, F.; Li, Y. F.; Hou, J. H. *Angew. Chem., Int. Ed.* **2011**, *50*, 9697.
- (20) Lee, J. K.; Ma, W. L.; Brabec, C. J.; Yuen, J.; Moon, J. S.; Kim, J. Y.; Lee, K.; Bazan, G. C.; Heeger, A. J. *J. Am. Chem. Soc.* **2008**, *130*, 3619.

- (21) Woo, C. H.; Beaujuge, P. M.; Holcombe, T. W.; Lee, O. P.; Fréchet, J. M. *J. Am. Chem. Soc.* **2010**, *132*, 15547.
- (22) Kouijzer, S.; Michels, J. J.; van den Berg, M.; Gevaerts, V. S.; Turbiez, M.; Wienk, M. M.; Janssen, R. A. *J. Am. Chem. Soc.* **2013**, *135*, 12057.
- (23) Heriot, S. Y.; Jones, R. A. L. *Nat. Mater.* **2005**, *4*, 782.
- (24) Jaczewska, J.; Budkowski, A.; Bernasik, A.; Raptis, I.; Raczkowska, J.; Goustouridis, D.; Rysz, J.; Sanopoulou, M. *J. Appl. Polym. Sci.* **2007**, *105*, 67.
- (25) Jaczewska, J.; Budkowski, A.; Bernasik, A.; Moons, E.; Rysz, J. *Macromolecules* **2008**, *41*, 4802.
- (26) Li, M.; Stelingen, N.; Michels, J. J.; Spijkman, M. -J.; Asadi, K.; Beerends, R.; Biscarini, F.; Blom, P. W. M.; de Leeuw, D. M. *Adv. Funct. Mater.* **2012**, *22*, 2750.
- (27) Krausch, G.; Dai, C. A.; Kramer, E. J.; Marko, J. F.; Bates, F. S. *Macromolecules* **1993**, *26*, 5566.
- (28) Jones, R. A. L. *Phys. Rev. E.* **1993**, *47*, 1437.
- (29) Geoghegan, M.; Jones, R. A. L.; Clough, A. S. *J. Chem. Phys.* **1995**, *103*, 2719.
- (30) Henderson, I. C.; Clarke, N. *Macromol. Theory Simul.* **2005**, *14*, 435.
- (31) Yan, L.-T.; Xie, X.-M. *Macromolecules* **2006**, *39*, 2388.
- (32) Michels, J. J. *ChemPhysChem* **2011**, *12*, 342.
- (33) Geoghegan, M.; Krausch, G. *Prog. Polym. Sci.* **2003**, *28*, 261.
- (34) Puri, S. *J. Phys.: Condens. Matter* **2005**, *17*, R101.
- (35) Binder, K.; Puri, S.; Das, S. K.; Horbach, J. *J. Stat. Phys.* **2010**, *138*, 51.
- (36) Björström, C. M.; Bernasik, A.; Rysz, J.; Budkowski, A.; Nilsson, S.; Svensson, M.; Andersson, M. R.; Magnusson, K. O.; Moons, E. *J. Phys.: Condens. Matter* **2005**, *17*, L529.
- (37) Björström, C. M.; Nilsson, S.; Magnusson, K. O.; Moons, E.; Bernasik, A.; Rysz, J.; Budkowski, A.; Zhang, F.; Inganäs, O.; Andersson, M. R. *Proc. SPIE* **2006**, *6192*, 61921X.
- (38) Björström, C. M.; Nilsson, S.; Bernasik, A.; Budkowski, A.; Andersson, M.; Magnusson, K. O.; Moons, E. *Appl. Surf. Sci.* **2007**, *253*, 3906.
- (39) Anselmo, A. S.; Lindgren, L.; Rysz, J.; Bernasik, A.; Budkowski, A.; Andersson, M. R.; Svensson, K.; van Stam, J.; Moons, E. *Chem. Mater.* **2011**, *23*, 2295.
- (40) Wodo, O.; GanapathySubramanian, B. *Comput. Mater. Sci.* **2012**, *55*, 113.
- (41) Saylor, D. M.; Kim, C.-S.; Patwardhan, C.-S.; Warren, J. A. *Acta Biomater.* **2007**, *3*, 851.
- (42) Kim, C.-S.; Saylor, D. M.; McDermott, M. K.; Patwardhan, D. V.; Warren, J. A. *J. Biomed. Mater. Res. Part B: Appl. Biomater.* **2009**, *688*.
- (43) Buxton, G. A.; Clarke, N. *Eur. Polym. Lett.* **2007**, *78*, 56006.
- (44) Clarke, N. *Eur. Phys. J. E* **2001**, *4*, 327.
- (45) Huang, C.; Olvera de la Cruz, M.; Swift, B. W. *Macromolecules* **1995**, *28*, 7996.
- (46) De Gennes, P. G. *J. Chem. Phys.* **1980**, *72*, 4756.
- (47) Jones, R. A. L.; Richards, R. W. *Polymers at Surfaces and Interfaces*; Cambridge University Press: Cambridge, U.K., 1999.
- (48) Henderson, I. C.; Clarke, N. *Macromol. Theory Simul.* **2005**, *14*, 435.
- (49) Binder, K.; Frisch, H. L. *Z. Phys. B Condens. Matter* **1991**, *84*, 403.
- (50) Yan, L.-T.; Xie, X.-M. *Macromolecules* **2006**, *39*, 2388.
- (51) Flory, P. *Principles of Polymer Chemistry*; Cornell University Press: Ithaca, NY, 1953.
- (52) Owens, D. K.; Wendt, R. C. *J. Appl. Polym. Sci.* **1969**, *13*, 1741.
- (53) Kwok, D. Y.; Neumann, A. W. *Adv. Colloid Interface Sci.* **1999**, *81*, 167.
- (54) Cahn, J. W.; Hilliard, J. E. *J. Chem. Phys.* **1958**, *28*, 258.
- (55) Cahn, J. W. *Acta Metall.* **1961**, *9*, 795.
- (56) Cook, H. E. *J. Chem. Solids* **1969**, *30*, 2427.
- (57) Cook, H. E. *Acta Metall.* **1970**, *18*, 297.
- (58) Huang, C.; Olvera de la Cruz, M. *Macromolecules* **1994**, *27*, 4231.
- (59) Kramer, E. J.; Green, P.; Palstrom, C. J. *Polymer* **1984**, *25*, 473.
- (60) Composto, R. J.; Kramer, E. J.; White, D. M. *Nature* **1987**, *328*, 234.
- (61) Calculated using ACD LABS Freeware (see: <http://www.acdlabs.com/resources/freeware/chemsketch/>)
- (62) According to Owens-Wendt theory.⁵² Unpublished work.
- (63) Various methods of determining surface energy contributions have been reviewed in: Żenkiewicz, M. *J. Achiev. Mater. Manuf. Eng.* **2007**, *24*, 137–145.
- (64) Schultz, J.; Tsutsumi, K.; Donnet, J. –B. *J. Colloid Interface Sci.* **1977**, *59*, 277.
- (65) We determined the disperse and polar part of the surface energy of F8BT, a polymer which is structurally similar to APFO-3. The polar part of this polymer was measured to be around 0.5 mN/m.
- (66) See for instance: Rubinstein, , M.; Colby, , R. H. *Polymer Physics*; Oxford University Press: Oxford, U.K., 2003.
- (67) Heffner, G. W.; Pearson, D. S. *Macromolecules* **1991**, *24*, 6295.
- (68) Monnaie, I.; Nies, E. L. F. et al. Submitted for publication.
- (69) Jones, R. A. L.; Norton, L. J.; Kramer, E. J.; Bates, F. S.; Wiltzius, P. *Phys. Rev. Lett.* **1991**, *66*, 1326.
- (70) Rysz, J.; Bernasik, A.; Ermer, H.; Budkowski, A.; Brenn, R.; Hashimoto, T.; Jedliński, J. *Europhys. Lett.* **1997**, *40*, 503.
- (71) Rysz, J.; Ermer, H.; Budkowski, A.; Lekka, M.; Bernasik, A.; Wróbel, S.; Brenn, R.; Lekki, J.; Jedliński, J. *Vacuum* **1999**, *303*.
- (72) Puri, S.; Binder, K. *J. Stat. Phys.* **1994**, *77*, 145.